Delineating loss sources within a linear cascade with upstream cavity and purge flow

Maxime Fiore*
Safran Aircraft Engine
CFD team CERFACS
Toulouse, France
Email: fiore@cerfacs.fr

Nicolas Gourdain
ISAE-Supaero
Dpt. of Aerodynamics,
Energetics and Propulsion
Toulouse, France
Email: nicolas.gourdain@isae-supaero.fr

Jean-François Boussuge
CFD team, CERFACS
Toulouse, France
Email: boussuge@cerfacs.fr

Eric Lippinois
Safran Aircraft Engine
Moissy-Cramayel, France
Email: eric.lippinois@safrangroup.com

Purge air is injected in cavities at hub of axial turbines to prevent hot mainstream gas ingestion into inter-stage gaps. This process induces additional losses for the turbine due to an interaction between purge and mainstream flow. This paper investigates the flow in a low-speed linear cascade rig with upstream hub cavity at a Reynolds number commonly observed in modern low pressure turbine stages by the use of numerical simulation. Numerical predictions are validated by comparing against experimental data available. Three different purge mass flow rates are tested using three different rim seal geometries. Numerical simulations are performed using a Large Eddy Simulation (LES) solver on structured grids. An investigation of the different mechanisms associated to turbine flow including cavity and purge air is intended through this simplified configuration. The underlying mechanisms of loss are tracked using an entropy formulation. Once described for a baseline case, the influence of purge flow and rim seal geometry on flow mechanisms and loss generation are described with the emphasis to obtain design parameters for losses reduction. The study quantifies loss generation due to boundary layer on wetted surfaces and secondary vortices developing in the passage. The analysis shows different paths by which purge flow and rim seal geometry can change loss generation including a modification of the shear layer between purge and mainstream, interaction with secondary vortices and a modification of the flow behavior close to hub compared to a smooth configuration. The study shows the influence of purge flow rate and swirl on the strengthening of secondary vortices in the passage and the ability of axial overlapping rim seal to delay the development of secondary vortices compared to simple axial gaps.

*Address all correspondence to this author.

1 Introduction

Necessary rotor-stator wheel space in low pressure turbines implies gaps often referred as cavities under the main flow passage in which hot turbine gas could be ingested and impinge rotor disks. Specific platform shapes are generally designed at the interface between two adjacent rows referred as the rim seal in order to prevent this phenomenon. However, these architectures are generally not sufficient to prevent overheating and potential rotor disks damages [1]. Some relative cold air is blown from the compressor to feed and seal turbine cavities and prevent partially hot-gas ingestion from the main annulus [2]. Due to the pressure difference across shaft sealing, part of this air called cavity purge flow blows into the mainstream through the rim seal. This low-momentum emerging flow interacts with the incoming main flow under a complex mixing process inducing losses that reduces turbine performance and needs to be correctly predicted in design phase [3]. The secondary system must provide a sufficient amount of purge flow to the cavity while keeping it to the minimum to reduce both mixing losses and penalty associated to bleed air at the compressor.

In the earlier studies of loss generation in a turbine, a convenient way to describe and measure loss was to split loss according to different contributions: profile, endwall and tip leackage losses for rotor rows. This approach made possible to develop models and correlations to get a better understanding of each physical phenomena and an estimate of the corresponding loss generated. However, these different phenomena are seldom independent as stated by Denton [4] and these studies were mainly focused on configurations where no cavity and purge flow were taken into account. For the last two decades, the influence of purge flow and more generally technological effects on aforementioned mechanisms

of losses and the new induced losses have become a key point for a more accurate estimation of the losses generated in a turbine. Furthermore, the mainstream passage optimization has become more and more difficult to achieve and the need for cooling system in the turbine has increased due to combustion chamber temperature increase. The first studies including purge flow showed a detrimental effect on turbine loss generation [5]. An increase of the horseshoe vortex process at blade leading edge was observed by Kost and Nicklas [6] and more generally of secondary flow generation in the passage. The mixing process at the rim seal interface and perturbed rotor secondary flows by purge flow in a stator-rotor configuration with cavity in-between were also reported by Reid et al. [7] as mechanisms inducing additional losses in the turbine. A potential reduction of losses could be achieved by promoting a swirled purge flow before to interact with the main annulus flow [7, 8]. However, the link between purge flow injection and the loss mechanisms remained difficult to establish [9]. The quantification of loss in these different studies was usually performed by comparing the evolution of actual total pressure or enthalpy to a hypothetical isentropic process. This approach was generally convenient from an experimental point of view since these quantities could be readily measured. However, in rotating rows, the relative stagnation pressure and the relative stagnation enthalpy can change as a result of changes in radius without there being any implied loss of efficiency [4]. At the same time, this leads to the conclusion that the only factor that changes loss generation is the departure from an isentropic flow and the loss can be seen as an entropy creation. From this statement, entropy formulation has become a good candidate to track loss generation for an adiabatic flow. Entropy generation as a measure of irreversibility in both flow and temperature field has gained from theoretical developments often referred under the name of Second-Law Analysis (SLA) that got its first applications in thermal systems [10]. For the considered Reynolds number and geometrical arrangement in gas turbine, entropy production needs to account for the turbulent contribution for an accurate prediction of entropy generation. Moore and Moore [11] proposed to account for the turbulent contribution using a Boussinesq assumption and an equivalent eddy viscosity similarly to the RANS approach. Orhan [12] was among the first to investigate loss mechanisms in an axial turbine cascade using Reynolds Averaged Navier-Stokes (RANS) simulation with SLA approach. Denton and Pullan [13] analyzed local entropy production rate in turbine using Unsteady RANS (URANS) simulations. However, Kopriva et al. [14] found that RANS simulations have generally not sufficient mesh grid refinement to properly evaluate entropy production. Furthermore, the estimation of turbulent entropy contribution is shown to be challenging for RANS models [15]. This paper describes the flow and related losses in a linear cascade with upstream hub cavity with different rim seal geometries and purge flow rates. The analysis is based on wall-resolved LES simulations where the dependence to turbulence modeling is lower compared to RANS approach in conjunction with the use of entropy to track the losses generated in the domain.

Table 1: Characteristics of the cascade rig

cascade details		nominal conditions	
Inlet blade angle	37.9 deg	Re	5.6 x 10^5
Outlet blade angle	66.3 deg	Ma	0.22
Axial chord C_x	75 mm	$\dot{m}_\mathrm{m}$	1.13 $kg.s^{-1}$
l_NGV/C_x	1.3	$p_\mathrm{tot,in}$ / p_out	1.035
Pitch/C_x	0.884	$\dot{m}_\mathrm{c}$ / $\dot{m}_\mathrm{m}$	0, 0.5, 1%
Tu	4%	$(p_\mathrm{ref}, T_\mathrm{ref})$	(101,325 Pa, 300 K)

The first part of this paper introduces the configuration and the numerical set up. The simulations performed are then compared against experimental data available. Once validated, the numerical simulation is used in conjunction with the entropy formulation to describe the mechanisms of loss in the linear cascade for a baseline case. Finally, the influence of purge flow rate and rim seal geometry are assessed and conclusions on the study are drawn.

2 Configuration and numerical methods

The configuration under study shown in Fig. 1 is a low-Mach linear cascade composed of five nozzle guide vane installed at Karlsruhe University, Germany. The rig is set in an open circuit which includes an upstream honeycomb settling chamber, a centrifugal blower and a Venturi pipe to target desired inflow conditions. Upstream of the blade leading edge, the rim seal is included in a cavity module linked to the test-section allowing to set different rim seal designs. The purge flow (c) is supplied to the cavity as a fraction of the mainstream flow (m), respectively $\dot{m}_\mathrm{c}/\dot{m}_\mathrm{m}$ = 0, 0.5 or 1% with a tangential component $\gamma = 45\ ^\circ$ with respect to span direction that mimic the entrainment effect of the rotor disk on the sealing flow in the cavity. The experimental turbulence level one axial chord upstream of the blade leading edge at mid-span was measured and provided $Tu \simeq 4\%$. Main rig characteristics are gathered in Tab. 1. In order to promote periodic conditions on lateral sections of each blade of the cascade, adjustable tailboards were moved along rig channel's wall. Their position was moved until reach a low discrepancy for the pressure distribution around the blade for the three inner blade. The tolerated pressure coefficient mismatch at mid-span between the three inner blades was set to 1%. This requirement was necessary to ensure that the comparison with numerical simulations for which only the central blade is simulated and periodic conditions are applied on the lateral sections would be compliant. Three different rim seal geometries were studied during the experiments. A first geometry with an axial clearance (simple gap) and two

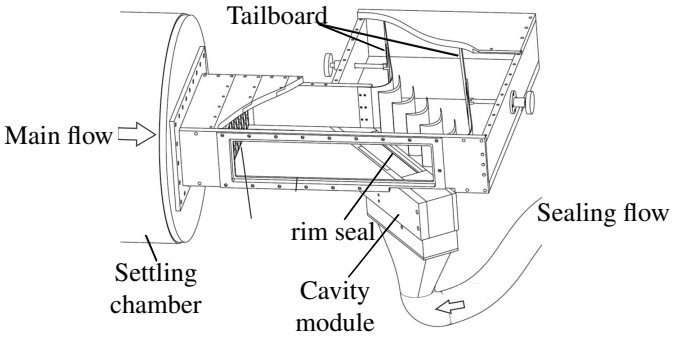

Fig. 1: Cascade rig. Adapted from Schuler et al. [16]

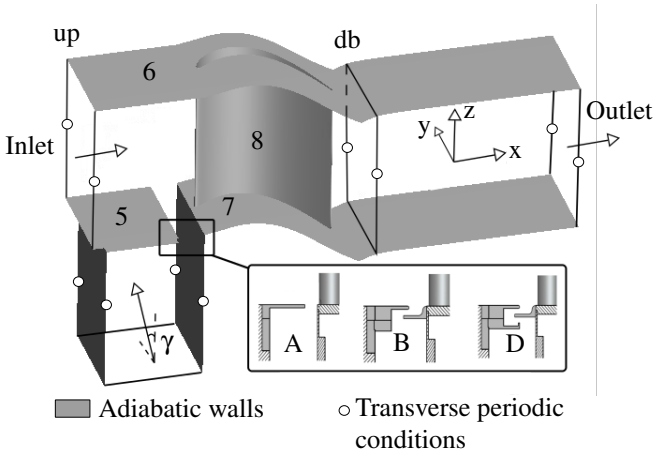

Fig. 2: Simulation domain including the boundary conditions

geometries using simple and double axial overlapping (referred as A, B and D in Fig. 2). In this paper, the different cases studied with the different geometries and purge flow rates will be denoted by a letter for the rim seal geometry (A: axial, B: simple overlapping, D: double overlapping) and a figure for the purge flow rate (0: 0%, 05: 0.5%, 1: 1%). For example, the configuration A05 stands for the axial rim seal geometry with 0.5% of the mainstream flow supplied in the cavity.

For the present study, the simulation domain is composed of one blade and aims at recovering the flow around central Nozzle Guide Vane (NGV) of the experimental test rig. The rim seal is set one axial chord-length (C_x) downstream of the inlet. The outlet is located 2 axial chord-length behind the blade trailing edge to avoid wave reflection issues. Navier-Stokes equations are solved using the ONERA CFD solver elsA [17] based on a cell-centred finite volume approach and a structured multi-block grid. Diffusive fluxes are computed with a second-order centred scheme. Convective fluxes are solved using a second order centred scheme with a low Jameson artificial viscosity [18] ($\kappa^4_{jam.} = 0.002$). The subgrid scale model is the Wall-Adapting Local Eddy-viscosity (WALE) [19] specifically designed to compute turbulent effects in wall-bounded flows by recovering the proper near-wall scaling for eddy viscosity. At the inlet, total pressure, total temperature and velocity direction profiles are applied according to experimental data without turbulence injection. Uniform velocity and temperature profiles are applied at the bottom of the cavity to meet desired purge flow 0, 0.5 or 1% of the mainstream flow. The purge flow is injected at a slightly lower temperature than the mainstream one ($T_c/T_m = 0.9$) to be able to follow how purge flow mixes with the main annulus one. The temperature gap between mainstream and cavity flow is generally higher in low pressure turbine typically $T_c/T_m \simeq 0.6$ for the first stage. The outlet is modelled by a throttle condition to target experimental mass flow by a variation of the throttle parameter ϕ,

$$p_{out}(t) = p_{ref} + \phi \dot{m}^2(t) \tag{1}$$

with p_{ref} a reference pressure taken as 101,325 Pa. The mesh is coarsened when approaching the outlet of the domain. This boundary condition has been coupled with a Navier-Stokes Characteristics Boundary Condition (NSCBC) [20].

Periodic conditions are applied on lateral sections and walls are considered as adiabatic (see Fig. 2). The flow domain is discretized with a multi-block approach using an O-4H meshing strategy for the NGV. Mesh generation in near-wall region has been set to fulfil recommendations for wall-resolved LES in a local body-fitted orthogonal system (see Fig. 3) which is $50 \leq s^+ \leq 150$; $n^+ \leq 1$; $15 \leq r^+ \leq 40$ [21] where s^+, n^+ and r^+ are the stream, wall-normal and spanwise non-dimensional coordinate on the blade wall. These recommendations have been lowered in span direction to capture streaks aligned with streamlines in near-wall region ($r^+ \leq 25$). Additionally, the mesh has been refined in the streamwise direction ($s^+ \leq 90$) (see Fig. 4 and 3). The time step is adapted to mesh resolution at walls $\Delta t^+ = \Delta t\ U_\infty/C_x = 10^{-5}$ (i.e. 1 500 time steps per axial chord length). The temporal integration is achieved with a Dual Time Step (DTS) approach based on an implicit backward Euler scheme with sub-iteration Newton's algorithm (second order accurate). The maximum CFL number based on the cubic root of the smallest cell volume in the domain remains lower than 11 in near-wall region.

3 Mesh dependency and comparison to experiment

Experimental results available are focused on the main annulus and comparison with numerical approaches is made on the simple axial clearance at various purge flow rate (A0, A05 and A1). The pressure coefficient C_p around the central blade and pressure loss coefficient downstream of the blade ζ are used for the comparison. These two quantities are defined as follows

$$C_p(x,z) = \frac{p_{blade}(x,z) - p_{tot,up}(z)}{p_{tot,db}(z) - p_{db}(z)} \tag{2}$$

$$\zeta(z) = \frac{p_{tot,up}(z) - p_{tot,db}(z)}{p_{tot,db}(z) - p_{db}(z)} \tag{3}$$

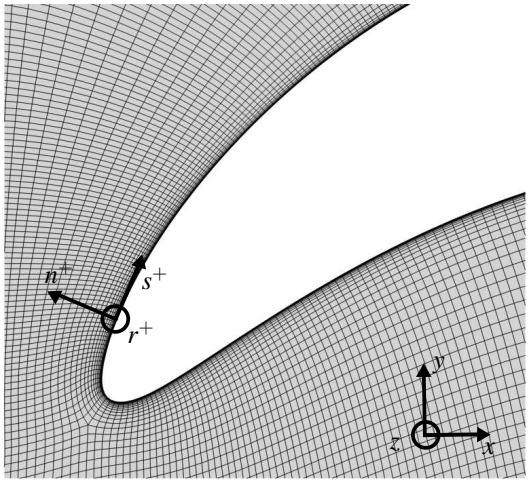

Fig. 3: Leading edge grid refinement at mid-span including Cartesian coordinates (x,y,z) and local body-fitted coordinates for wall-resolved requirements (s^+, n^+, r^+)

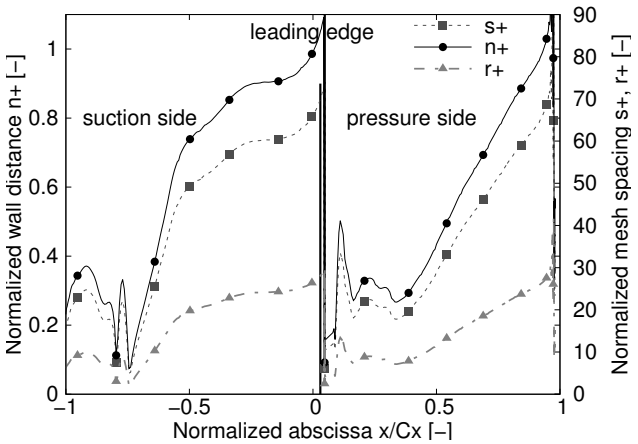

Fig. 4: Mid-span averaged grid dimension at wall, configuration A05

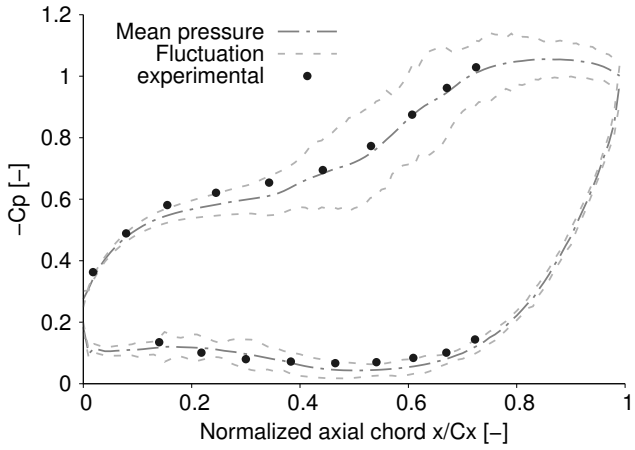

Fig. 5: Pressure coefficient and domain of fluctuation at 4% span height, configuration A05

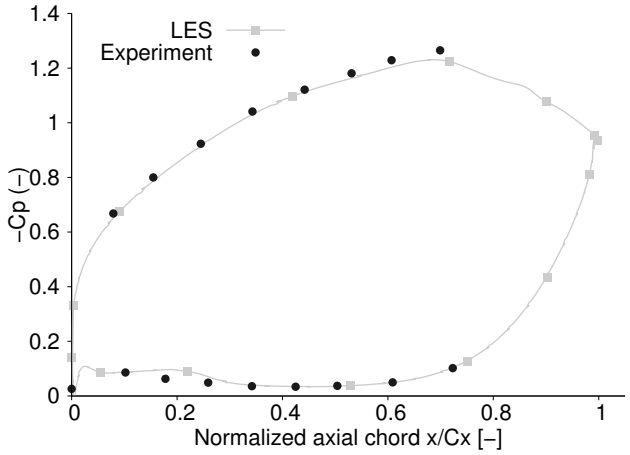

Fig. 6: Pressure coefficient around blade at mid-span, configuration A05

where p_{tot} and p are the total and static pressure around blade. The pressure upstream (up) and downstream (db) of the blade (see Fig. 2) at a spanwise position (z) have been averaged in the transverse direction (y). These pressure coefficient profiles helps to evaluate the ability of the solver to capture the blade loading that is known to vary with the amount of purge flow especially close to the wall. The pressure loss coefficient profile indicates the strength and position of secondary flows also known to be influenced by the purge flow especially in the first half height of the main annulus.

In order to assess grid convergence, a simulation has been performed using a finer grid where all three near-wall characteritic length have been decreased: $s^+ \leq 80$, $n^+ \leq 0.8$ and $r^+ \leq 15$. Mesh refinement has been mainly performed in the spanwise direction since this parameter have been shown to strongly influence LES simulation quality [22] and fewer in the streamwise direction. Indeed, the streaks that are to be captured in wall-resolved LES simulations are elongated structures in the streamwise direction [23] with fewer variations compared to the wall-normal and span directions. The final mesh is composed of around 110 Mcells compared to the 60 Mcells mesh used for the study. The pressure coefficient around the blade at 4 and 50% (A05 configuration) and the pressure loss coefficient downstream of the blade (A0, A05, A1 configurations) obtained from the experiments and time-averaged LES simulations are shown in Fig. [5-9]. The mesh dependency is assessed on the pressure loss coefficient downstream of the blade for the A05 configuration (see Fig. 8). The two meshes have low discrepancy along the blade height with maximum discrepancy around 1% except at the location of the two main loss peaks at $z/l_{\text{NGV}} = 0.3$ and $z/l_{\text{NGV}} = 0.7$ where the discrepancy can be locally around 4%. Despite these local differences, the results between standard and refined meshes are in relatively good agreement.

Compared to the experiments, the pressure coefficient profiles on the pressure side are well predicted at the different span height by the LES simulation with the standard grid. On the suction side, LES profiles underpredict pressure coefficient locally of 8%. Regarding pressure loss coefficient

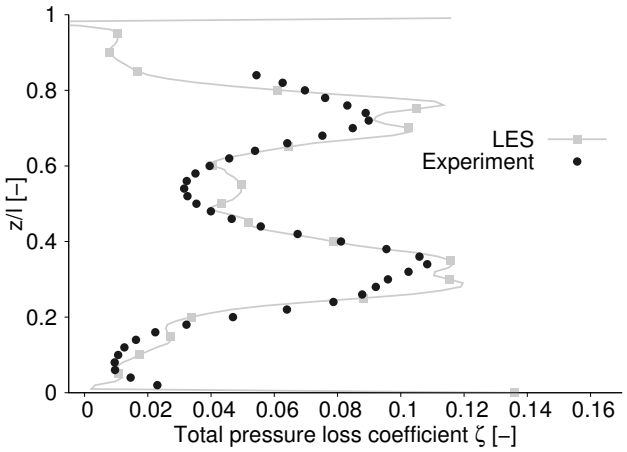

Fig. 7: Total pressure loss coefficient downstream of the blade, configuration A0

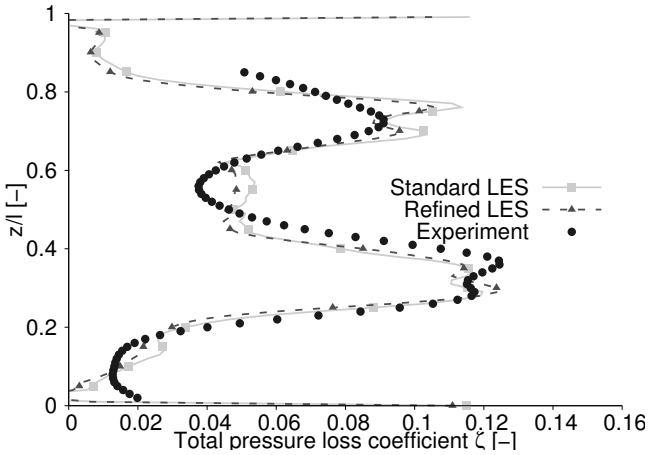

Fig. 8: Total pressure loss coefficient downstream of the blade, configuration A05 including the pressure loss coefficient for the standard grid used during the study (60 Mcells) and the refined grid (110 Mcells)

downstream of the blade, position and amplitude of the lowest pressure peak mainly induced by hub passage vortex is well captured but slightly overpredicted around 5% in terms of amplitude. Mid-span area separating the two main loss pressure loss displays an additional pressure peak. After additional post processing, this pressure peak was attributed to a separation bubble occurring mainly at mid-span due to the adverse pressure gradient initiated at the throat ($x/C_x = 0.7$) and will be discussed in Sec. 8. Also, the top pressure loss peak mainly due to shroud passage vortex is overestimated. Despite some discrepancy in the results, the numerical approach is able to predict loss pattern with the two main loss peaks separated by a low pressure loss central channel both in terms of position and amplitude. In addition, the numerical simulation has shown unaffected pressure loss profile downstream blue of the blade when $z/l_{\mathrm{NGV}} \geq 60\%$ for the different purge mass flow rates. The lower pressure peak amplitude increases with the increased purge mass flow rate promoting an influence of purge flow on hub passage vortex

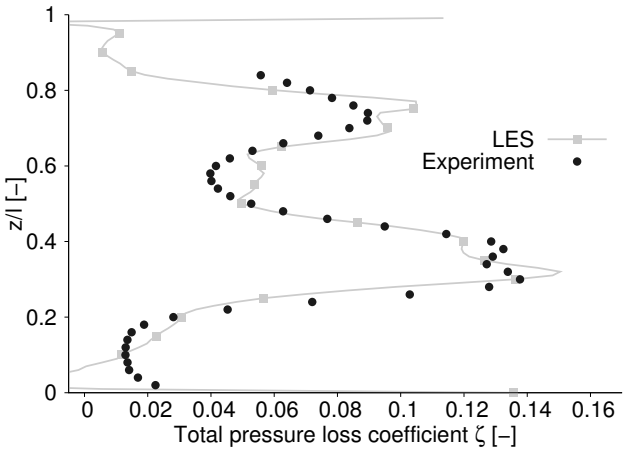

Fig. 9: Total pressure loss coefficient downstream of the blade, configuration A1

while the region between $z/l_{NGV} = 0$ and 0.3 is relatively unaffected by the purge flow. These results show the ability of the LES simulation to capture turbine annulus flow features when purge flow is added and give more confidence in the flow behaviour that will be further depicted in next sections.

4 Entropy generation as a measure of losses

Denton [4] showed that the only rational measure of loss in an adiabatic machine is entropy creation. A transport equation for specific entropy can be derived from thermodynamic principles and Navier-Stokes equations. A detailed demonstration is given in Greitzer et al. [24]. For RANS and LES approaches where part of the turbulence is modelled, additional treatments must be performed to account for the modelled part. Moore and Moore [11] proposed to model the entropy related to velocity and temperature fluctuations by an equivalent turbulent viscosity and mean flow velocity/temperature gradients leading to the following equation in RANS formalism:

$$\begin{aligned}\frac{\partial}{\partial t}\left(\overline{\rho}\overline{S}\right)+\frac{\partial}{\partial x_i}\left(\overline{\rho}\overline{u_i}\overline{S}+\frac{\overline{q}}{\overline{T}}\right) &= \mu_{eff}\left(\frac{\partial\overline{u_i}}{\partial x_j}+\frac{\partial\overline{u_j}}{\partial x_i}\right)\frac{1}{\overline{T}}\frac{\partial\overline{u_i}}{\partial x_j} \\ &\quad+\frac{\lambda_{eff}}{\overline{T}^2}\left(\frac{\partial\overline{T}}{\partial x_j}\right)^2 \\ &= S_{\mathrm{visc}} + S_{\mathrm{therm}}\end{aligned} \tag{4}$$

where $\mu_{\mathrm{eff}} = \mu + \mu_{\mathrm{turb}}$ and $\lambda_{\mathrm{eff}} = \lambda + \lambda_{\mathrm{turb}}$ are the effective viscosity and conductivity, q is the heat flux and $\bar{\cdot}$ refers to the mean quantity in RANS formalism. For current LES simulation, part of the turbulence is held by the mean flow and the equivalent turbulence viscosity due to unresolved eddies is held by the subgrid scale model. In the context of turbomachinery, the notion of secondary flow and related losses is often defined as the flow normal to the circumferentially averaged mean flow direction. For a better account of secondary

flows, it is then convenient to write the different entropy contributions in the polar streamline coordinates (stream, cross and radial components) [9]. In the current study of linear cascade and more generally in high hub-to-tip ratio, it is convenient to approximate polar stream line coordinate by local Cartesian coordinate denoted (s, c, r) where at each point of the domain the main direction is aligned with flow direction. Next sections will be devoted to characterize the flow behaviour in the linear cascade and cavity in conjunction with the entropy formulation to track related losses. For the sake of clarity, the surfaces and flow region studied are numbered in Fig. 2 according to the corresponding section number. In addition, unsteady flow feature associated with physical phenomena are described.

The first section describes the flow associated to the boundary layer developing on the shroud and interaction with the blade leading edge especially horseshoe vortex process and subsequent developing secondary flows in the passage. Since the study of losses on the blade surface including endwall has been deeply studied, it will make possible as a first step to assess the ability of LES simulation in conjunction with entropy approach to correctly reproduce physical mechanisms and related loss generation. The study will be then led close to the hub with the additional rim seal and mixing layer at the interface between mainstream and cavity compared to the shroud. In the following sections, when no special mention is made, the different figures refers to the axial rim seal geometry with intermediate purge flow 0.5% (configuration A05). The main direction abscissa (x) has been non-dimensionalized by the axial chord length and 0 correspond to the blade leading edge abscissa while trailing edge is 1. The interface between the main annulus and cavity extends from x/C_x = -0.25 to x/C_x = -0.04 (see Fig. 10 bottom). Entropy generation is non dimensionalized by a reference temperature at the inlet of the domain (T_{ref}) multiplied by the flow time scale (C_x/u_x) then divided by the dynamic pressure at the inlet of the blade ($1/2\ \rho u_x^2$) which gives $S_{.,\text{ad}} = T_{\text{ref}} S_. /(0.5\rho u_x^3/C_x)$ where . refers to the considered contributing term. In the following figures, the normalized entropy is plotted.

5 Incoming boundary layer

A boundary layer develops at the hub from the inlet to the rim seal-left corner and from rim seal right corner to outlet while at shroud the boundary layer can develop from inlet to the blade leading edge. To extract entropy generation associated to boundary layer, the boundary layer thickness must be evaluated over the domain at hub and shroud. In the study, the criterion proposed by Michelassi et al. [25] is used to estimated boundary layer thickness. This criterion is based on a vorticity criterion (ω) with an arbitrary threshold ($\omega_{\text{threshold}}$) defined as

$$\omega_{\text{threshold}} = \omega_{\text{min}} + 0.01\ (\omega_{\text{max}} - \omega_{\text{min}}). \qquad (5)$$

The simulation domain has been discretized in subsequent axial domains, a volume integration of each term and total entropy production has been performed for each of the sub-domains (see Fig. 10). Figure 11 displays entropy related to ($\partial u_s/dr$) gradient contribution all along the domain $S(\text{visc}, \partial u_s/\partial r)$. Each of the contribution to entropy (gradient directions) along the domain will be plotted against total production $S(\text{visc}, \text{tot})$ to give the reader the relative contribution of each term. In addition, the same post-processing bounded to hub and shroud boundary layer is applied. Total entropy production and entropy production due to ($\partial u_s/dr$)

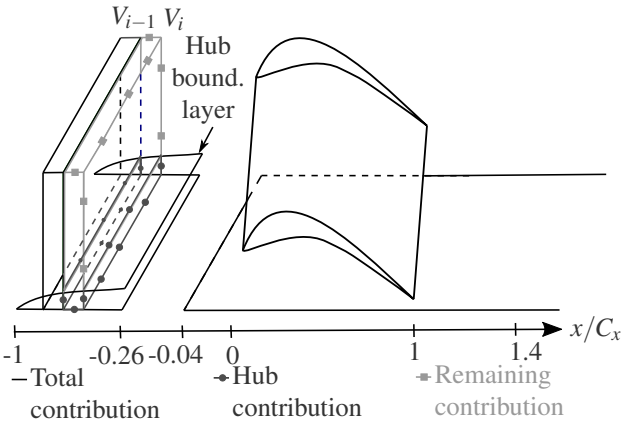

Fig. 10: Example of a simulation domain discretized in axial subvolumes V_i (black lines). For a simple configuration where only the hub boundary layer is considered, V_i can be split in a subvolume associated to the hub boundary layer (dark grey lines with dots) and a remaining domain out of boundary layers that is simply the subvolume V_i minus the subvolume associated to the hub boundary layer (light grey lines with squares)

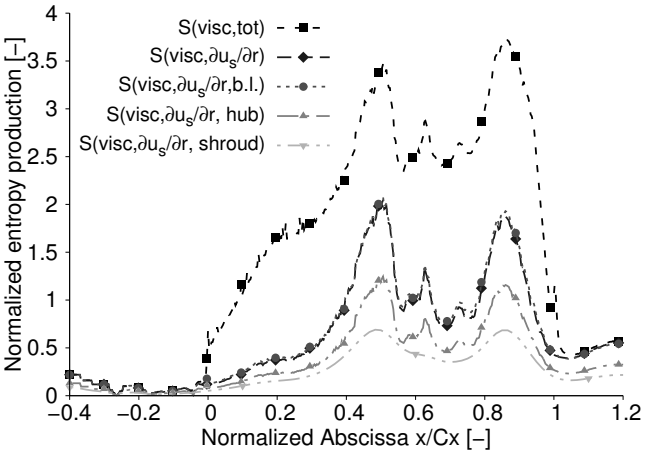

Fig. 11: Viscous entropy production along the domain $S(\text{visc}, \text{tot})$, within hub $S(\text{visc}, \text{hub})$, shroud boundary layers $S(\text{visc}, \text{shroud})$ and in hub-shroud boundary layers $S(\text{visc}, \text{b.l.})$ with the restriction to $\partial u_s/\partial r$ contribution that is the hub/shroud wall-normal velocity gradient, configuration A05

gradients are at same level from inlet to rim seal left corner x/C_x = -0.25. Furthermore, this contribution is limited to boundary layer since entropy production due to $(\partial u_s/dr)$ gradients all over the domain and the contribution limited to boundary layer $S(\text{visc}, \text{b.l.})$ are equal. This observation indicates the development of a boundary layer at the hub and shroud that leads to wall-normal gradients $(\partial u_s/dr)$ and generates the majority of entropy along this portion of the domain.

6 Secondary flow generation at shroud

The interaction of shroud boundary layer with the blade leading edge is first studied. This configuration that can be considered as a blade including endwall has been deeply studied by numerous authors [6, 26, 27]. The scope of this subsection is to verify that the main mechanisms previously reported are also observed in this configuration. This section will be then used to draw the differences with the hub where the endwall is partially replaced by the cavity upstream of the blade including emerging purge flow. The flow at the inlet

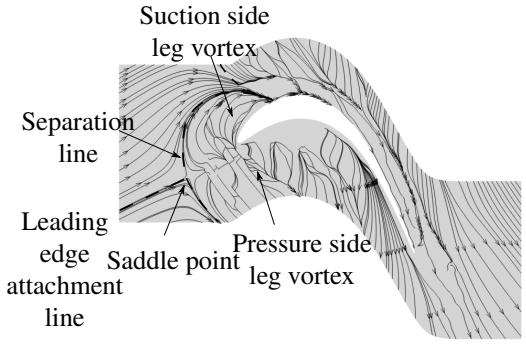

Fig. 12: Streak lines obtained from friction vectors at shroud, configuration A05

is introduced with a tangential component that mimics the deviation done by an upstream rotor row. Figure 12 shows streak lines obtained from friction vectors at the shroud endwall. When the shroud boundary layer approaches the blade at around half axial chord length from the leading edge, the streak lines bifurcate as they approach the saddle point due to an increasing static pressure from the blade leading edge potential effect and low momentum of shroud boundary layer compared to the free stream one. The boundary layer detaches along the separation line inducing the formation of vortical flow structures orthogonal to mainstream flow direction immediately downstream of the separation line. These rolling structures travel until blade leading edge (see Fig. 13). Dynamical Mode Decomposition (DMD) performed on the instantaneous field at the shroud is used and made possible to isolate amplified modes showed in Fig. 14. These modes are related to the rolling up of vortical structures developing upstream of the leading edge and impacting blade leading edge at St = (f D)/u_{bl} = (650 0.02)/30 = 0.4, where f is the frequency, D the distance from saddle point to blade leading

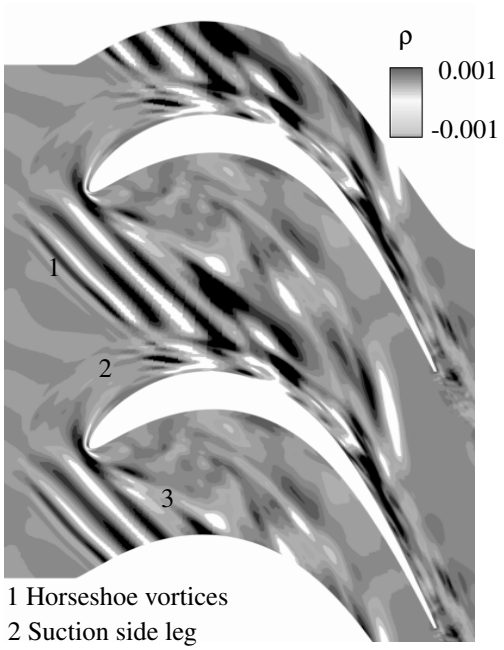

Fig. 13: Density modes related to horseshoe vortex process at the shroud, configuration A05

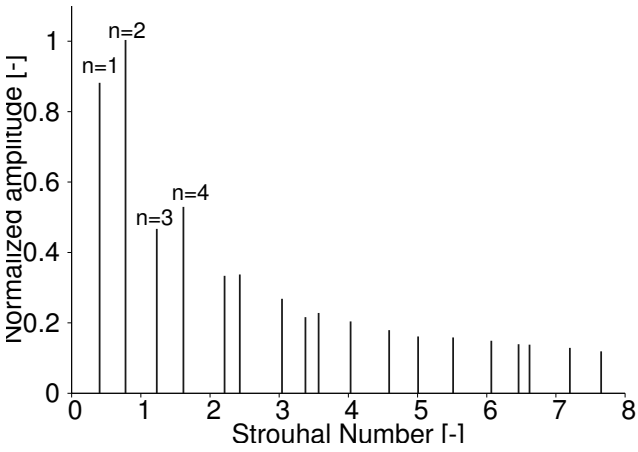

Fig. 14: Density spectrum from DMD based on shroud skin temporal signal, configuration A05

edge (see Fig. 14). This frequency corresponding to the vortex shedding depends on the boundary layer edge velocity u_{bl} and equivalent diameter of blade leading edge [28]. This vortex structure termed as horseshoe vortex is split by the blade leading edge and propagates downstream in the passage on both pressure and suction side forming two legs (see Fig. 12). Suction side leg remains attached to the blade while pressure side leg travel along inter-blade channel due to pressure gradient from pressure side of one blade to suction side of adjacent blade. Downstream of the pressure side separation line, the new-born endwall boundary layer is very thin and skewed towards suction side since the incoming flow is mainly entrained by pressure side leg [29]. Far from endwall the equi-

librium between pitchwise pressure gradient and centrifugal forces on the fluid element being broken down close to endwall due to low momentum boundary layer [30]. Entropy production remains low from saddle point to the blade leading edge at shroud and downstream of the blade leading edge where the new-born shroud boundary layer develops in the passage. A first peak of entropy production between $x/C_x = 0.4$ and $x/C_x = 0.5$ is observed due to the growing pressure side leg that drives the new-born shroud boundary layer and induces additional friction on the shroud endwall (see Fig. 11). At nearly half axial chord length, the suction side and pressure side leg merge together in the region where the two separation lines meet close to blade suction side and initiate the formation of the passage vortex (see Fig. 12). The entropy production at the shroud tends to lower in this region. On the blade suction side, the flow is less accelerated in the boundary layer than in the free stream. A negative spanwise pressure gradient is induced from the endwall to free stream. Figure 15 shows streak lines around the blade suction side and pressure side. Near the shroud on the blade suction side, a streak line deviation can be observed that indicates the migration of the passage vortex on the blade suction side due to spanwise pressure gradient. The migration is characterized by a three-dimensional turbulent flow travelling along blade and skewed [30]. Pressure and suction side leg merge

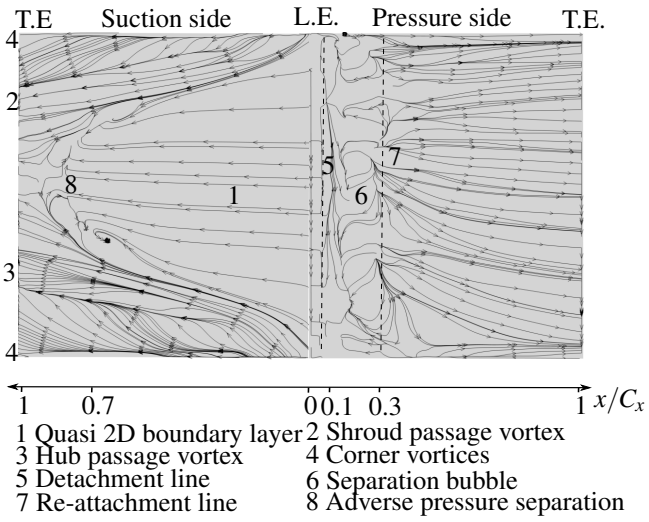

Fig. 15: Streak lines on blade suction and pressure side, configuration A05

induces the formation of an additional vortex structures that remains close to shroud called corner vortex that can be observed on the streamlines of Fig. 15 and Fig. 16. This vortical structure strengthens with the axial coordinate inducing additional friction close to the shroud and entropy production with a second peak between $x/C_x = 0.8$ and $x/C_x = 1.0$ (see Fig. 11).

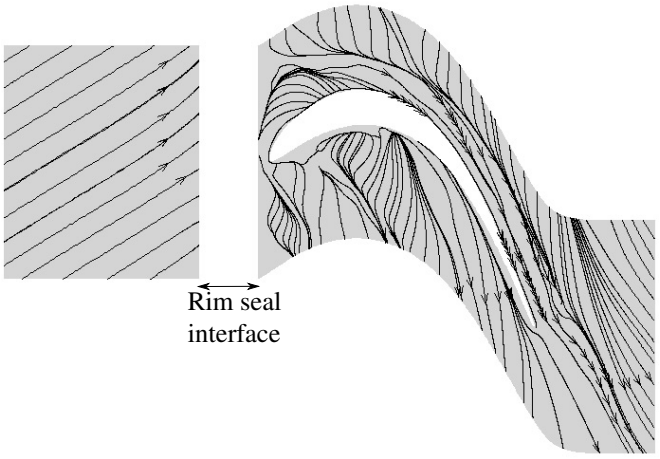

Fig. 16: Streak lines at hub

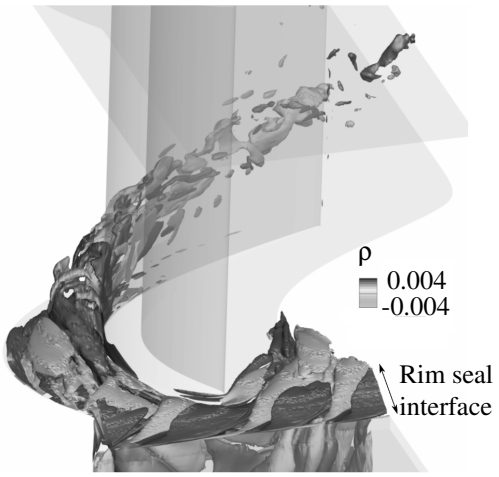

Fig. 17: Three-dimensional DMD modes related to the first harmonics of Kelvin-Helmholtz instability, configuration A05

7 Rim seal influence and secondary flow generation at hub

The mainstream flow close to the hub that separates at the rim seal left corner interacts with the flow in the rim seal. The flow in the rim seal is entrained by the mainstream flow and lead to a clockwise recirculation zone in the rim seal. The flow in the rim seal is accelerated to the main annulus one over a short layer at a location close to rim seal left corner. At this interface, a shear layer is induced due to the azimuthal and axial velocity gap. DMD was performed on the instantaneous three-dimensional solution close to the rim seal interface and was used to isolate amplified modes represented in Fig. 17. Coherent cylindrical structures orthogonal to the stream velocity can be observed and characterize the development of Kelvin-Helmholtz instability due to the shear layer. Since the cavity flow emerges with a lower temperature than the mainstream one, Fig. 18a shows that the mixing is driven by the instability and keep the coherent structure related to the instability (alternating hot and cold streaks are

observed at the rim seal interface). These structures are partially deviated downwards into the cavity at the rim seal right corner for the structures facing the blade potential effect and are convected in the main annulus when at the center of the passage between two vanes (see Fig. 19). The flow struc-

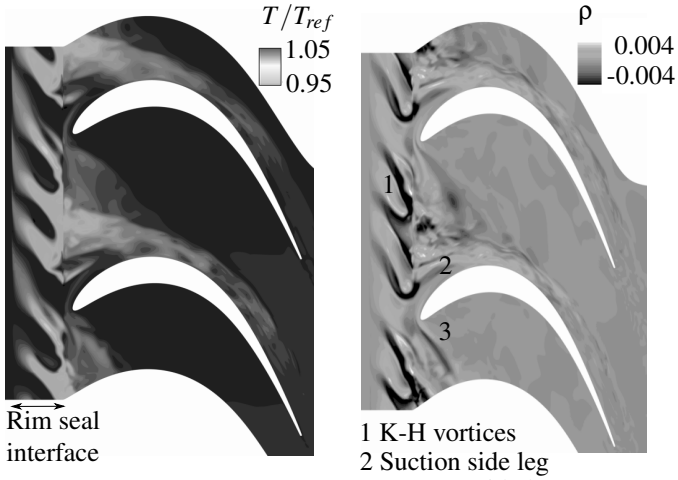

Fig. 18: Total temperature distribution on the hub surface, at the rim seal interface (a) and density modes related to Kelvin-Helmholtz instability (K-H) at the hub (b)

tures ingested into the cavity progressively vanish when going further downstream in the cavity (see Fig. 19a). Since the flow is partially ingested into the cavity, the conservation of mass for the cavity is fulfilled by blowing of cavity flow into mainstream. This mass flow amount is even higher when purge flow is provided to cool down the cavity. The blowing process into the mainstream is made at the center of inter-blade channel and close to the suction side where static pressure is lower (see Fig. 20). Due to the rim seal at hub, the horse shoe roll-up process can only be initiated between rim seal right corner and the blade leading edge. At shroud, the rolling process was initiated with low momentum shroud boundary layer. At hub, the rolling process is mainly initiated with low momentum emerging cavity flow. This rolling process is made at the same rate than at shroud (horse shoe vortex process) but includes lower spatial extent modes related to the Kelvin-Helmholtz instability (see Fig. 21). The different mechanisms leading to the formation of the passage vortex at shroud are similar at hub except that secondary flows are fed by both endwall boundary and the emerging cavity flow. Since the mechanisms are similar at hub and shroud downstream of the blade leading edge, a similar entropy production with a strong contribution of pressure side leg and further downstream the corner vortex is observed. However, secondary vortices being strengthened at hub due to purge flow, the vortical structures have larger secondary kinetic energy than the one emerging from the horse shoe

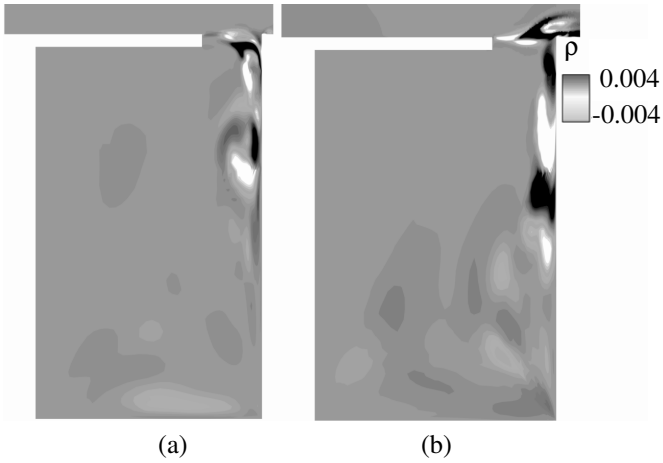

Fig. 19: Two-dimensional DMD modes related to Kelvin-Helmholtz instability base on a meriodional plane extraction face to blade leading edge (a) and at the center of the passage (b), configuration A05

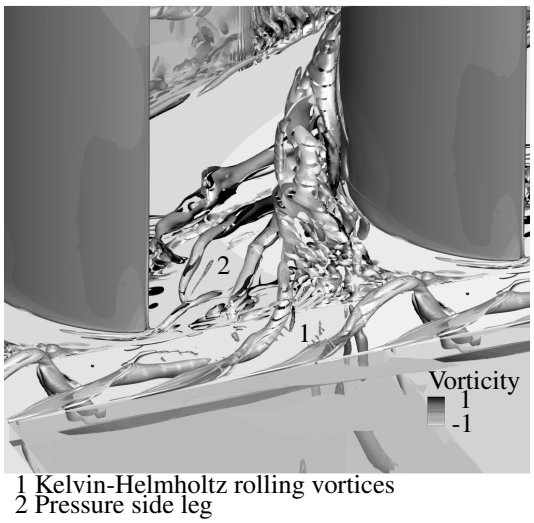

Fig. 20: Horse shoe vortex and interaction with cavity flow based on a iso Q-criterion $Q = 10^6$ colored by streamwise vorticity, configuration A05

vortex process at shroud, leading to additional friction at hub and more entropy production as observed in Fig. 11.

8 Blade flow feature

Figure 15 shows streak lines related to the blade pressure side and suction side. On the blade pressure side, the laminar boundary layer separates at around ten percent chord length due to the adverse pressure gradient and re-attaches at around thirty percent axial chord length inducing a closed separation bubble on most of the span. The pressure side is almost unaffected by secondary structures and the flow is essentially two-dimensional. The boundary layer developing on the blade suction side is essentially laminar until the separation bubble occurring at 70% chord length. The surface oil-flow visualization reported by Hodson and Dominy [31]

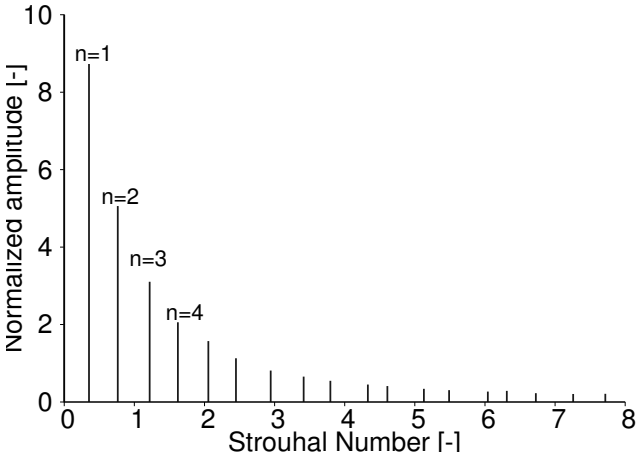

Fig. 21: Density spectrum from DMD based on hub skin temporal signal, configuration A05

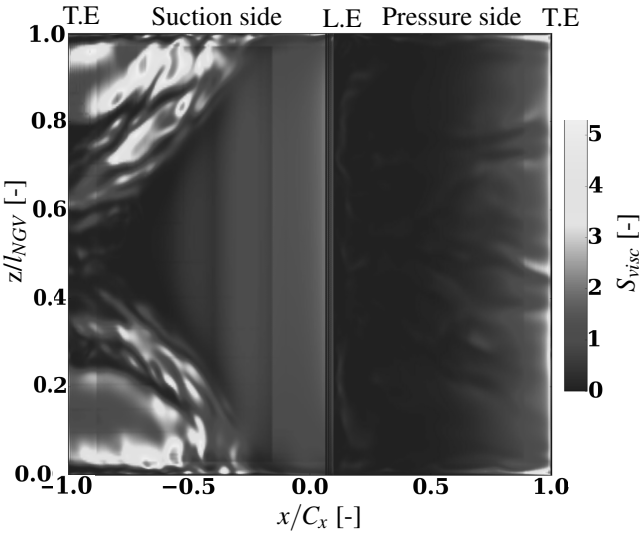

Fig. 22: Viscous entropy production at a constant distance from the blade wall ($y^+ \simeq 30$), configuration A05

on a linear cascade at lower Reynolds Re = 1.8×10^5 and low free stream turbulence showed similar flow topology around the blade. The experimental study of Abu Ghanam and Shaw [32] on the transition process of the boundary layer over a flat plate at various Reynolds number, axial pressure gradient and free stream turbulence can give some informations on the boundary layer on blade suction side. At the considered Reynolds number based on the chord Re $= 5 \times 10^5$, for no free stream turbulence (no turbulence injected at the inlet of the LES simulation), the boundary layer may remain laminar until Re $\sim 10^6$ (here the assumption is made that the blade suction side can be approximated by a flat plate, no curvature effect and similar surface roughness compared to the experiments of Abu Ghanam and Shaw [32]). However, since the experiments provided turbulence intensity levels of around Tu = 4%, and for the considered Reynolds number, the boundary layer may be transitional/turbulent since the transition to turbulence can decrease of a factor 10 for the Reynolds number (Re $\sim 10^5$). This may cancel the separation bubble due to adverse pressure gradient since a turbulent boundary layer is less prone to separate due to more momentum close to the wall provided by turbulence. This explanation is supported by no constant pressure coefficient on the aft portion of the blade suction side and no additional pressure loss peak at mid-span downstream of the blade in the experiments compared to the current LES simulation. Figure 22 shows entropy production above the blade wall ($y^+ \simeq 30$). Entropy is mostly produced on the blade suction side. Entropy production is almost constant on this part of

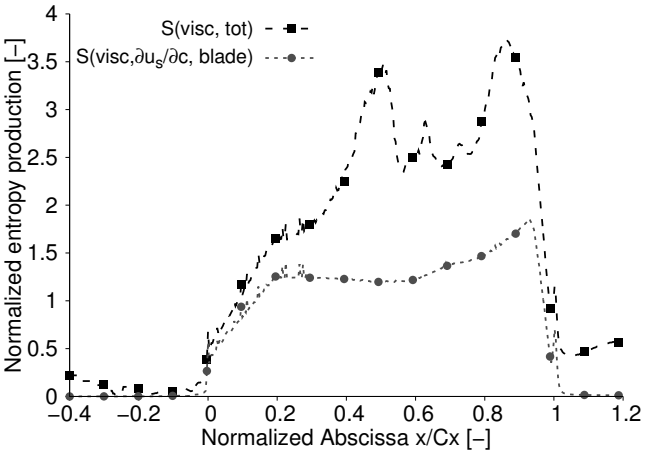

Fig. 23: Viscous entropy production along the domain S(visc,tot), within blade boundary layer S(visc,$\partial u_s/\partial c$, blade) where $\partial u_s/\partial c$ contribution is the blade wall-normal velocity gradient, configuration A05

the blade and is due to wall-normal gradients as it can be observed in Fig. 23. As observed in previous section, the streak lines around the blade made possible to analyse the radial migration of hub and shroud passage vortices on the blade and corner vortex close to endwall (see Fig. 24). Similarly to the pressure side of the horse shoe vortex and corner vortex close to the hub and shroud surfaces, secondary vortices induce additional entropy production by a local friction process on the blade suction side at location where secondary vortices travel. When the contributions of the hub, shroud and blade boundary layer are factored out from the total entropy contribution in the passage, the remaining domain contains the contribution of the secondary vortices out of the boundary layers (see $S(\text{visc}, \text{out bound. layer})$ in Fig. 25) The entropy production is mainly performed in an isentropic fashion close to the center of vortical structures where the secondary kinetic energy held by secondary vortices is dissipated. The development of vortical structures in the passage induces unsteadiness at the same location where these patterns travel. At the shroud, unsteadiness observed on the blade suction side corresponds to the locations where passage and corner vortices travel. The blade loading fluctuations occur at a frequency corresponding to the horseshoe vortex process. At the hub, Fig. 5 shows the pressure coefficient around the

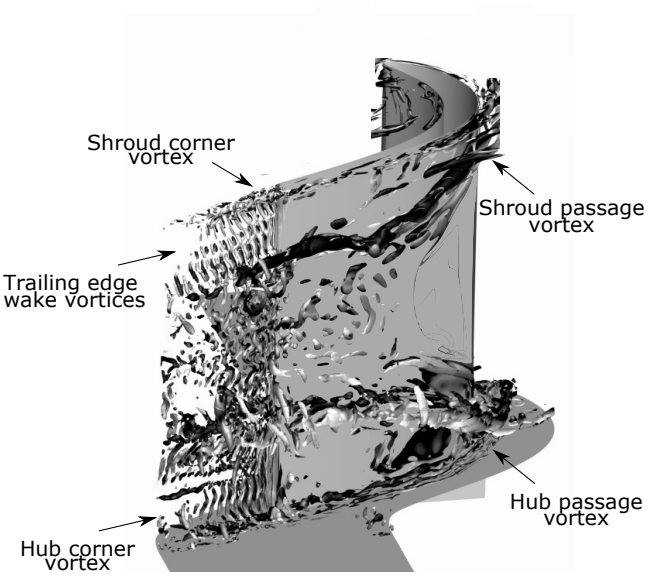

Fig. 24: Sight from downstream to upstream of secondary flow in the passage obtained using iso Q-criterion $Q = 10^6$ colored by vorticity for the configuration A05. The shroud is omitted

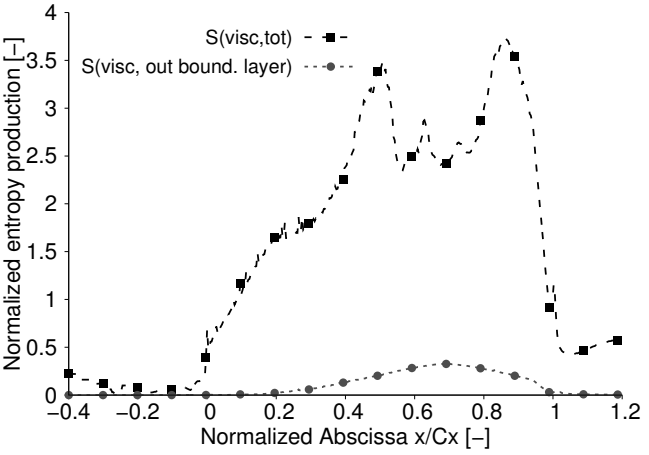

Fig. 25: Viscous entropy production along the domain S(visc,tot) and contribution out of the hub, shroud and blade boundary layers where secondary vortices are alleged to produce entropy, configuration A05

at hub due to Kelvin-Helmholtz instability. This could be achieved by reducing tangential and axial velocity gap between mainstream and rim seal flow by increasing swirl in the cavity or longer axial rim seal arms to increase rim seal axial flow component.

9 Flow downstream of the blade

A peak of entropy production can be observed at the trailing edge due to trailing shed vortex process. Entropy production out of boundary layers due to wakes, declining secondary vortices are restricted to a region close to the blade trailing edge since the level of total entropy production and within boundary layer at hub and shroud becomes quickly equal downstream of the trailing edge (see Fig. 11) Figure 26 shows total pressure and stream vorticity at 25%

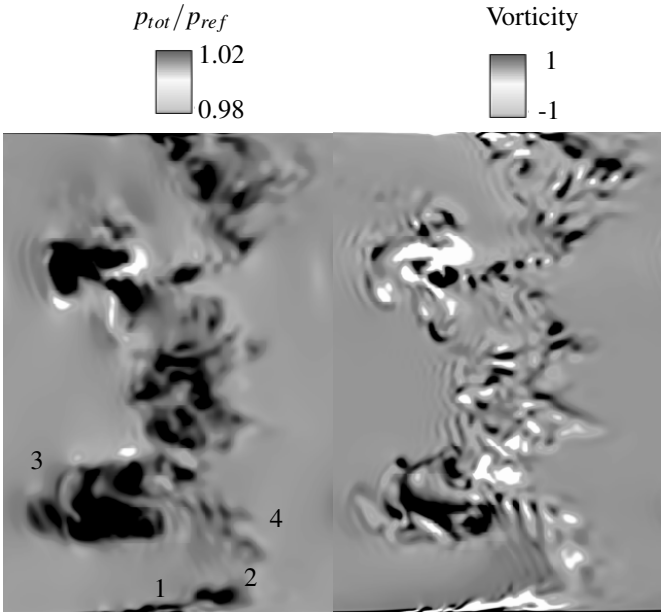

1 Boundary layer
2 Corner vortex
3 Passage vortex
4 Trailing shed vortices

Fig. 26: Non-dimensionalized total pressure and streamwise vorticity 25% chord length downstream of the blade, configuration A05

blade at 4% blade span. The maximum pressure fluctuation envelope $p_{\text{mean}} \pm \max(p_{\text{RMS}})$ around the mean temporally averaged value p_{mean} becomes important on the blade suction side at an axial coordinate corresponding to the migration of passage vortex. Blade unsteadiness close to the hub is mainly driven by the horseshoe vortex process and Kelvin-Helmholtz instability at higher frequency. At the hub, since the secondary flows are partially fed by the cavity flow, thermal stress also occurs on blade suction side where secondary vortices travel. The shedding process due to horseshoe process is difficult to reduce except using Karman kind devices like fillets. A reduction of shear layer intensity close to the rim seal could reduce unsteadiness on the blade suction side

axial chord length downstream of the blade where the experimental pressure measurements have been performed. The analogy proposed by Denton [4] can be used to describe the total pressure loss downstream of the cascade: local entropy generated or equivalently loss in the cascade can be seen as "smoke". Once created by an irreversibility in the flow, the "smoke" cannot be destroyed and is convected downstream through the cascade. The concentration of "smoke" downstream of the cascade can be seen as the accumulation of losses generated upstream and measured in current case as a loss of total pressure compared to inlet total pressure. Close to hub and shroud, areas of low pressure can be observed due to the boundary layer developing on these wetted sur-

faces (1) and corner vortex at hub and shroud (2). Out of hub and shroud boundary layers, part of the losses are related to profile losses with pressure and suction side blade boundary layer contributions. In addition to this contribution, the trailing shed vortex process occurs at blade trailing edge (4) over all span. Hub and shroud passage vortex (3) comes to be superimposed to these last contributions with the two main loss peaks observed at $z/l_{NGV} = 0.3$ and $z/l_{NGV} = 0.7$ in Fig. [7-9] used for the comparison against experiments. The detrimental effect of secondary flows and cavity at hub regarding a smooth configuration at shroud is confirmed with stronger corner and passage vortex at hub than shroud (see Fig. 26 and [7-9]). The integrated pressure loss coefficient for the different rim seal geometry as a function of the purge flow rate is provided in Fig. 27. The increased purge flow rate has a detrimental effect on the loss generated in the cascade for all rim seal geometries. The axial overlapping geometries induce less losses compared to the simple gap. The next two sections are devoted to describe the contributions influenced by the purge flow rate and rim seal geometry explaining these differences in pressure loss downstream of the blade.

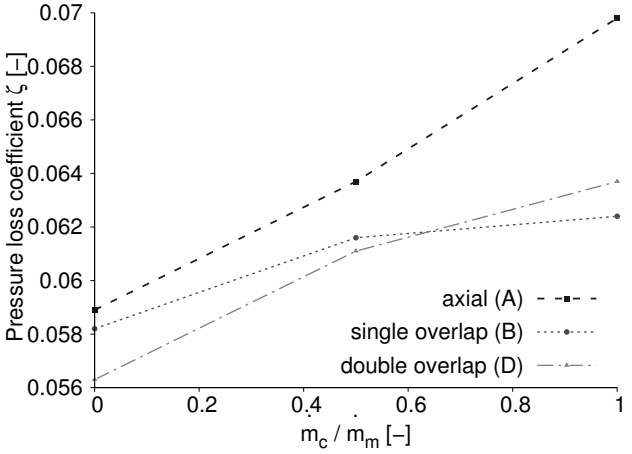

Fig. 27: Integrated pressure coefficient downstream of the blade for the different rim seal geometries depending on the purge flow rate supplied

purge flow rate does not modify entropy production. The main differences are shown to be in the blade passage. Figure 29 shows entropy production related to the hub boundary layer. When purge flow is increased, entropy production is increased especially at locations related to secondary flows development: pressure side leg for the first peak of entropy and corner vortex for the second peak. This observation shows that an increase of purge flow leads to more energetic secondary vortices and higher friction close to the hub. This statement is also observed in Fig. [30-31] that shows the influence of purge flow on entropy production around the blade boundary layer and due to secondary vortices out of boundary layer. According to these two figures, additional purge flow induces more entropy production in the aft portion of the blade after $x/C_x = 0.7$ that was attributed to secondary flow friction on the blade in Sec. 8 related to the flow around the blade. The level of entropy production out of boundary layers due to secondary vortices also increases which support the idea of strengthened secondary vortices. Figure 30 also shows that entropy production due to laminar blade boundary layer is almost not influenced by purge flow rate since entropy generation doesn't change along the first 70% chord length.

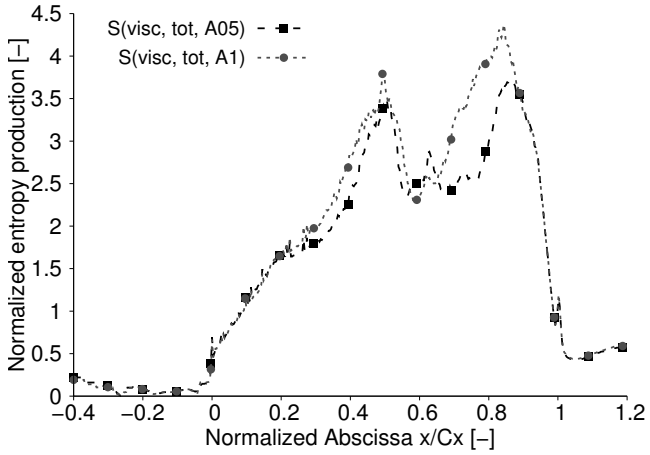

Fig. 28: Entropy generation along the simulation domain for configuration A05 and A1

10 Influence of purge flow rate

The main mechanisms and areas of entropy generation have been described in last sections for the axial rim seal and intermediate purge flow rate (configuration A05). The purpose of this section is to determine the influence of the amount of purge flow on these mechanisms and entropy generation for the axial rim seal. Figure 28 shows entropy production along the simulation domain at intermediate and high purge flow rate for the axial rim seal geometry (configurations A05 and A1). The entropy generation increases with an increased purge flow rate. The purge flow shows no influence on loss generation on upstream domain, as well as downstream of the blade. Even at the rim seal interface,

11 Influence of rim seal geometry

This section is focused on the second parameter of the study that is the rim seal geometry. The comparison of rim seal geometry based on axial gap, simple and double axial overlapping is led at an intermediate purge flow rate (A05, B05 and D05 configurations). The axial overlapping geometries promote an intense recirculation zone that homogenizes the flow at the rim seal interface compared to simple axial gaps. A main consequence is that the main annulus ingested flow (negative radial velocity close to rim seal interface) is made over a lower axial extent for overlapping geometries than axial geometry (see Fig. 32a for axial ge-

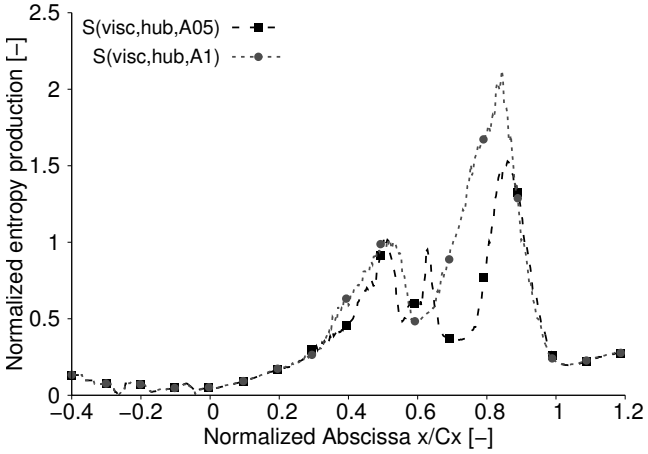

Fig. 29: Entropy generation at hub boundary layer along the simulation domain for configuration A05 and A1

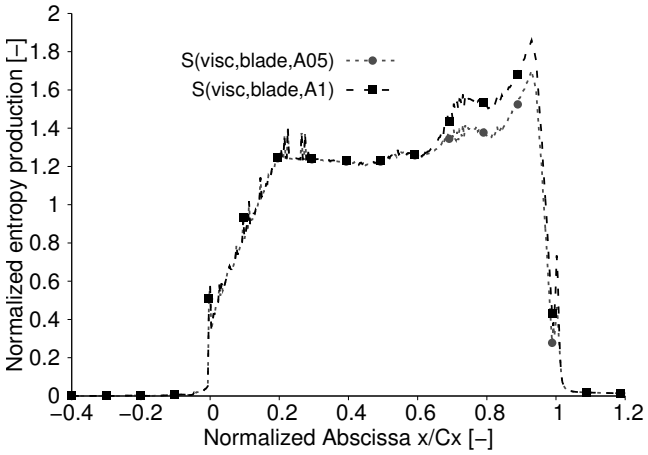

Fig. 30: Entropy generation at blade boundary layer along the simulation domain for configuration A05 and A1

ometry and Fig. 32b for single overlapping geometry). The cavity/rim seal flow emerges earlier in the axial direction and closer to blade leading edge (see Fig. 33). This induces an earlier development and strengthening of the horse shoe vortex, pressure side of the horse shoe vortex for the simple gap geometry compared to overlapping ones. The radial migration of secondary vortices along blade suction are initiated early for the axial rim seal (see Fig. 32). At the rim seal interface, the entropy production associated to azimuthal and axial velocity gap between the main and rim seal flow is lower for the overlapping geometries. This is due to the local recirculation zone for overlapping geometries that reduces the shear compared to the axial geometry (see Fig. 34). Regarding the entropy production at the hub and related to the secondary vortices, the entropy production for axial overlapping geometries is lower than simple axial gap since the secondary vortices have developed later in the passage. Entropy production due to hub is mainly reduced at the first peak of losses that was described to be mainly induced by the growing of pressure side leg horseshoe vortex (see Fig. 35). Downstream of the pressure and suction side

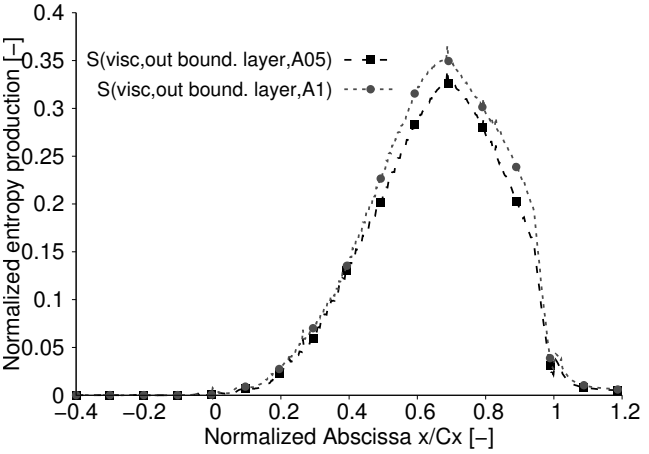

Fig. 31: Entropy generation due to secondary losses along the simulation domain for configuration A05 and A1

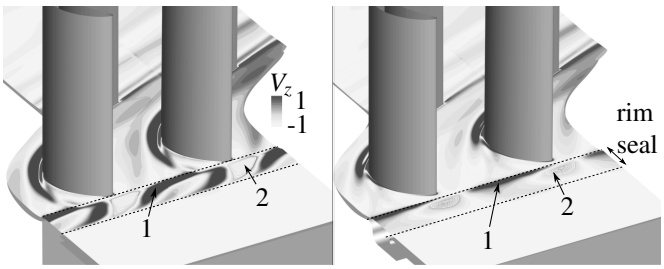

Fig. 32: Radial cut close to the hub colored by the non-dimensional radial velocity for axial A (a) and single overlapping B geometry (b)

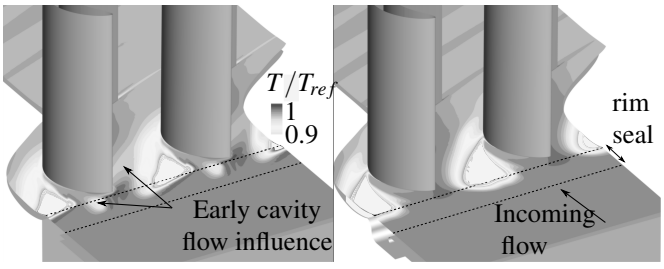

Fig. 33: Radial cut close to the hub colored by the non-dimensional temperature for axial A (a) and single overlapping geometry B (b)

leg merge, secondary vortices have decreased secondary kinetic energy. The entropy production on the blade due to a friction process of secondary vortices and entropy production out of boundary layers is reduced for overlapping rim seals compared to the axial rim seal (see Fig. 36). The observation that secondary vortices are weaker for overlapping rim seals regarding to the axial one is also confirmed out of boundary layers since the entropy production related to the mixing of vortical structures close to their center of rotation

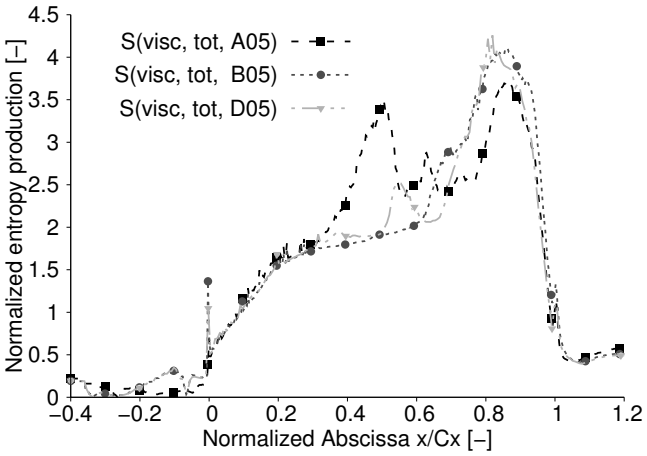

Fig. 34: Entropy generation along the simulation domain for A (axial), B (simple) and D (double overlapping) rim seals

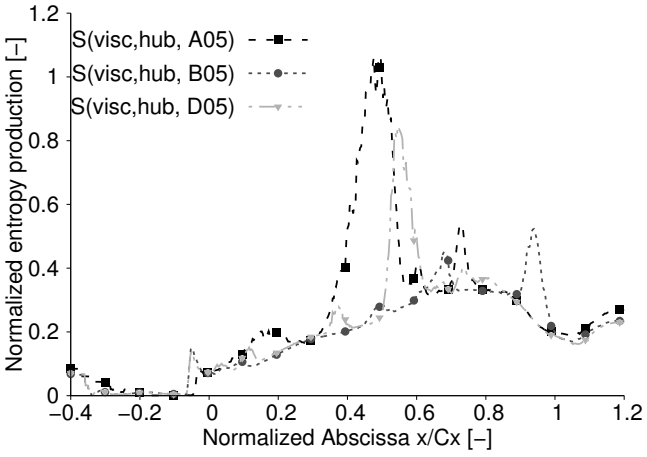

Fig. 35: Entropy generation at hub boundary layer along the simulation domain for A (axial), B (simple) and D (double overlapping) rim seals

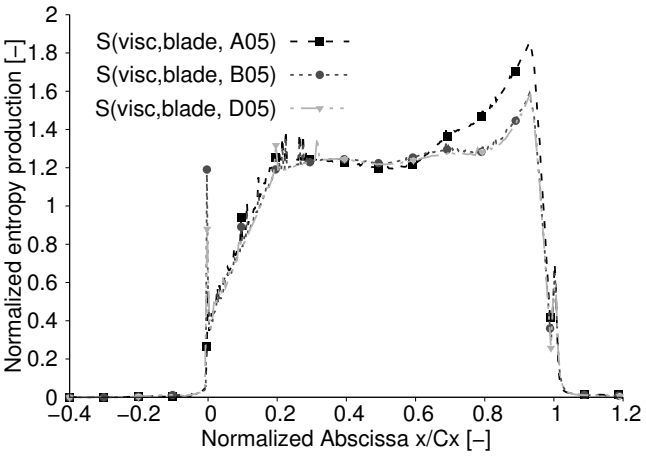

Fig. 36: Entropy generation at blade boundary layer along the simulation domain for A (axial), B (simple) and D (double overlapping) rim seals

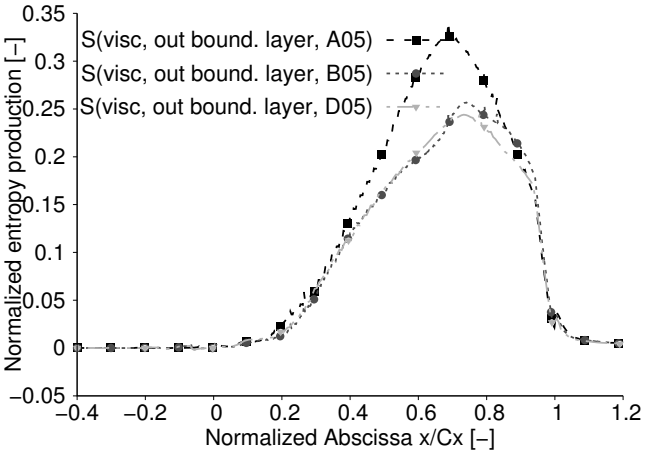

Fig. 37: Entropy generation due to secondary losses along the simulation domain for A (axial), B (simple) and D (double overlapping) rim seals

is also decreased (see Fig. 37).

12 Conclusion

LES simulation of a linear cascade including an upstream cavity and rim seal have been conducted. Since no rotating disk was taken into account as in a real configuration, the effect of the potential pressure asymmetry generated by downstream blade could be isolated from rotating disk pumping effect. An entropy formulation has been applied as a measure of loss generation in the cascade. At the shroud, horse shoe vortices impact periodically the blade leading edge and separates into two legs. The leg travelling along the passage from pressure to suction side of the adjacent blade and strengthens by an entrainment process of the new-born shroud boundary layer. The two legs merge on the blade suction side and initiate the passage vortex that migrates radially and a corner vortex close to the shroud endwall. At the hub, the development of secondary vortices is similar to the shroud with an additional feeding process of the pressure side leg of the horse shoe vortex by the cavity flow leading to more energetic structures. Two mechanisms of loss associated to secondary vortices have been identified based on the entropy approach: a dissipation process close to their center of rotation under a nearly isentropic process where secondary kinetic energy is dissipated, a friction process of the secondary vortices on the surfaces of the main annulus mainly the hub, shroud and blade suction side. The unsteady phenomena observed in the linear cascade are related to the horse shoe vortex process at hub, shroud and trailing shed vortex process at the blade trailing edge. The Kelvin-Helmholtz instability due to the shear layer at the rim seal interface is an additional unsteady phenomenon at the hub. The fluctuations related to theses two phenomenon can be observed around the blade where secondary vortices travel and downstream of the blade with the passage vortex. An increased purge flow rate supplied in the cavity is shown to increase the secondary kinetic energy of secondary vortices dissipated in the passage and induce more losses. More com-

plex axial overlapping geometries compared to simple axial gaps promote a delayed development of secondary vortices in the passage and as a consequence less loss related to the secondary vortices occurs.

Acknowledgments

The authors are thankful to Safran Aicraft Engines for technical support and having funded this research project, to ONERA for licensing Cerfacs to use code elsA (ONERA-Airbus-Safran property). Numerical post-processing have been performed using the free python-based Library Antares. Part of this work was performed using HPC resources from GENCI - [CCRT-CINES-IDRIS] (Grant 2017-[a0022a06074]). Experimental data were obtained within the EU research project Main Annulus Gas Path Interactions (MAGPI), AST5-CT-2006-030874.

Nomenclature

Latin letters:

C_x	m	axial chord-length
C_p		pressure coefficient
l_{NGV}	m	blade height
k	$m^2.s^{-2}$	turbulent kinetic energy
Ma		Mach number
$\dot{m}$	$kg.s^{-1}$	mass flow rate
q	$kg.m^{-2}.s^{-2}$	heat flux
R_e		Reynolds number
S	$kg.m^{-1}.s^{-2}$	entropy
Tu		turbulence intensity
u	$m.s^{-1}$	velocity
(x,y,z)	m	cartesian coordinates
(s,c,r)	m	local stream coordinates

Greek letters:

γ	deg	sealing flow angle, $tan^{-1}(u_z/u_x)$
ω	s^{-1}	vorticity
ζ		total pressure loss coefficient
λ	$kg.m.s^{-3}.K^{-1}$	thermal conductivity
κ		artificial viscosity coefficient
ϕ		throttle parameter
μ	$kg.m^2.s^{-1}$	dynamic viscosity

Subscripts and superscripts:

c	cavity
m	main annulus
ref	reference state
tot	total quantity
turb	turbulent
therm	thermal
visc	viscous

References

[1] Chupp, R. E., Hendricks, R. C., Lattime, S. B., and Steinetz, B. M., 2006. "Sealing in Turbomachinery". *Journal of Propulsion and Power,* **22**(2), pp. 313–349.

[2] Moore, A., November 30–December 5,1975. "Gas Turbine Engine Internal Air Systems: A Review of the Requirements and the Problems". In ASME 1975 Winter Annual Meeting: GT Papers, p. V001T01A001. Houston, Texas, USA.

[3] Pau, M., Paniagua, G., Delhaye, D., de la Loma, a., and Ginibre, P., 2010. "Aerothermal Impact of Stator-Rim Purge Flow and Rotor-Platform Film Cooling on a Transonic Turbine Stage". *Journal of Turbomachinery,* **132**(2), p. 021006.

[4] Denton, J. D., 1993. "Loss Mechanisms in Turbomachines". *Journal of Turbomachinery,* **115**(4), p. 621.

[5] Marini, R., and Girgis, S., May 14-17, 2007. "The Effect of Blade Leading Edge Platform Shape on Upstream Disk Cavity to Mainstream Flow Interaction of a High-Pressure Turbine Stage". In ASME Turbo Expo 2007: Power for Land, Sea, and Air. Montreal, Canada.

[6] Kost, F., and Nicklas, M., 2001. "Film-cooled turbine endwall in a transonic flow field: Part I - Aerodynamic measurements". *Journal of Turbomachinery,* **123**(4), pp. 709–719.

[7] Reid, K., Denton, J., Pullan, G., Curtis, E., and Longley, J., May 8-11,2006. "The Effect of Stator-Rotor Hub Sealing Flow on the Mainstream Aerodynamics of a Turbine". In ASME Conference Proceedings, Vol. 2006, pp. 789–798. Barcelona, Spain.

[8] Zlatinov, M. B., Sooi Tan, C., Montgomery, M., Islam, T., and Harris, M., 2012. "Turbine Hub and Shroud Sealing Flow Loss Mechanisms". *Journal of Turbomachinery,* **134**(6), p. 061027.

[9] Laskowski, Gregory M Kopriva, J., Michelassi, V., and Shankaran, S., 2011. "Entropy production calculation for turbulent shear flows and their implementation in cfd codes". *Journal of Turbomachinery,* **26**(1), pp. 672–680.

[10] Bejan, A., 1982. "Second-Law Analysis in Heat Transfer and Thermal Design". *Advances in Heat Transfer*.

[11] Moore, J., and Moore, J. G., 1983. "Entropy Production Rates From Viscous Flow Calculations: Part I - A Turbulent Boundary Layer Flow". In Volume 1: Turbomachinery, p. V001T01A032.

[12] Orhan, O., 2014. "Investigation of the Effect of Turbulence on Entropy Generation in Turbomachinery". PhD thesis, Middle East Technical University, Ankara, Turkey.

[13] Denton, J., and Pullan, G., 2012. "A Numerical Investigation Into the Sources of Endwall Loss in Axial Flow Turbines". In Volume 8: Turbomachinery, Parts A, B, and C, p. 1417.

[14] Laskowski, G. M., Kopriva, J., Michelassi, V., and Shankaran, S., 2016. "Future Directions of High-Fidelity CFD for Aero-Thermal Turbomachinery Research , Analysis and Design". In AIAA, pp. 1–30.

[15] Jin, Y., and Herwig, H., 2014. "Turbulent flow and heat

transfer in channels with shark skin surfaces: Entropy generation and its physical significance". *International Journal of Heat and Mass Transfer,* **70**, pp. 10–22.

[16] Schuler, P., Dullenkopf, K., and Bauer, H.-J., 2011. "Investigation of the Influence of Different Rim Seal Geometries in a Low-Pressure Turbine". *Volume 7: Turbomachinery, Parts A, B, and C*, pp. 715–729.

[17] Cambier, L., Heib, S., and Plot, S., 2013. "The Onera elsA CFD software: input from research and feedback from industry". *Mechanics & Industry,* **14**(3), pp. 159–174.

[18] Jameson, A., Schmidt, W., and Turkel, E., 1981. "Numerical solutions of the Euler equations by finite volume methods using Runge-Kutta time-stepping schemes". *AIAA paper*.

[19] Nicoud, F., and Ducros, F., 1999. "Subgrid-scale stress modelling based on the square of the velocity gradient tensor Subgrid-scale stress modelling based on the square of the velocity gradient tensor". *Flow, Turbulence and Combustion,* **62**(3), pp. 183–200.

[20] Poinsot, T. J., and Lelef, S. K., 1992. "Boundary conditions for direct simulations of compressible viscous flows". *Journal of Computational Physics,* **101**(1), pp. 104–129.

[21] Gourdain, N., Sicot, F., Duchaine, F., and Gicquel, L., 2014. "Large eddy simulation of flows in industrial compressors: a path from 2015 to 2035". *Philosophical Transactions of the Royal Society A: Mathematical, Physical and Engineering Sciences,* **372**(2022), pp. 20130323–20130323.

[22] R. Pichler, Y. Zhao and R. D. Sandberg, V. Michelassi, R. Pacciani, M. M., and Arnone, A., June 11–15 2018. "LES and RANS analysis of the end-wall flow in a linear LPT cascade with variable inlet conditions, Part I: Flow and secondary vorticity fields". In ASME Turbo Expo 2018: Turbomachinery Technical Conference and Exposition. Oslo, Norway.

[23] Tucker, P. G., 2011. "Computation of unsteady turbomachinery flows: Part 2-LES and hybrids". *Progress in Aerospace Sciences,* **47**(7), pp. 546–569.

[24] Greitzer, E. M., Tan, C. S., Graf, M. B., 2007. *Internal flow: concepts and applications (Vol. 3).*, cambridge ed.

[25] Michelassi, V., Martelli, F., Dénos, R., Arts, T., and Sieverding, C. H., June 2-5,1998. "Unsteady heat transfer in stator-rotor interaction by two equation turbulence model". *ASME 1998 International Gas Turbine and Aeroengine Congress and Exhibition*. Stockholm, Sweden.

[26] Sharma, O. P., and Butler, T. L., 1987. "Predictions of Endwall Losses and Secondary Flows in Axial Flow Turbine Cascades". *Journal of Turbomachinery,* **109**(86), p. 229.

[27] Sieverding, C. H., 1985. "Recent Progress in the Understanding of Basic Aspects of Secondary Flows in Turbine Blade Passages". *Journal of Engineering for Gas Turbines and Power,* **107**(2), p. 248.

[28] Cui, J., Nagabhushana Rao, V., and Tucker, P., 2015. "Numerical Investigation of Contrasting Flow Physics in Different Zones of a High-Lift Low-Pressure Turbine Blade". *Journal of Turbomachinery,* **138**(1), p. 011003.

[29] Harrison, S., 1989. "Secondary Loss Generation in a Linear Cascade of High-Turning Turbine Blades". In Volume 1: Turbomachinery, p. V001T01A021.

[30] Mahmood, G. I., and Acharya, S., 2007. "Experimental Investigation of Secondary Flow Structure in a Blade Passage With and Without Leading Edge Fillets". *Journal of Fluids Engineering*.

[31] Hodson, H. P., and Dominy, R. G., 1987. "Three-Dimensional Flow in a Low-Pressure Turbine Cascade at Its Design Condition". *Journal of Turbomachinery,* **109**(2), p. 177.

[32] Abu-Ghannam, B. J., and Shaw, R., 1980. "Natural Transition of Boundary Layers". *Journal Mechanical Engineering Science,* **22**(5), pp. 213–228.